The Evolution of Size and Merger Fraction of Submillimeter Galaxies across $1 < z \lesssim 6$ as Observed by JWST

Jian Ren [ID],[1,2] F. S. Liu [†] [ID],[1,3,4] Nan Li [†],[1,2,4] Pinsong Zhao,[5,1] Qifan Cui [ID],[6,1] Qi Song,[1,2] Yubin Li,[1,2] Hao Mo,[1,3,4] Hassen M. Yesuf,[7] Weichen Wang,[8] Fangxia An [ID],[9] and Xian Zhong Zheng[10,9]

[1] National Astronomical Observatories, Chinese Academy of Sciences, 20A Datun Road, Chaoyang District, Beijing 100101, China

[2] Key Laboratory of Space Astronomy and Technology, National Astronomical Observatories, Chinese Academy of Sciences, 20A Datun Road, Chaoyang District, Beijing 100101, China

[3] Key Laboratory of Optical Astronomy, National Astronomical Observatories, Chinese Academy of Sciences, 20A Datun Road, Chaoyang District, Beijing 100101, China

[4] School of Astronomy and Space Science, University of Chinese Academy of Science, Beijing 100049, China

[5] Kavli Institute for Astronomy and Astrophysics, Peking University, Beijing 100871, China

[6] Shanghai Key Lab for Astrophysics, Shanghai Normal University, Shanghai 200234, China

[7] Key Laboratory for Research in Galaxies and Cosmology, Shanghai Astronomical Observatory, Chinese Academy of Sciences, 80 Nandan Road, Shanghai 200030, China

[8] Dipartimento di Fisica G. Occhialini, Università degli Studi di Milano-Bicocca, Piazza della Scienza 3, I-20126 Milano, Italy

[9] Purple Mountain Observatory, Chinese Academy of Sciences, 10 Yuanhua Road, Nanjing 210034, China

[10] Tsung-Dao Lee Institute and Key Laboratory for Particle Physics, Astrophysics and Cosmology, Ministry of Education, Shanghai Jiao Tong University, Shanghai 200240, China

ABSTRACT

Precise tracking of the growth in galaxy size and the evolution of merger fractions with redshift is vital for understanding the formation history of submillimeter galaxies (SMGs). This study investigates these evolutions over a broad redshift range ($1 < z \lesssim 6$), using a sample of 222 SMGs with a median redshift of $z = 2.61^{+0.89}_{-0.82}$ identified by ALMA and JCMT, enhanced by the advanced imaging capabilities of the JWST/NIRCam and MIRI. We find significant evolution in effective radii (R_e) in rest-frame V-band ($R_e \propto (1 + z)^{-0.87 \pm 0.08}$) and near-infrared (NIR) band ($R_e \propto (1 + z)^{-0.88 \pm 0.11}$), with the NIR size evolution resembling that of massive star-forming galaxies at lower redshift. Visual inspections reveal a major merger fraction of $24.3 \pm 3.7\%$ and an interaction fraction of up to $48.4 \pm 11.1\%$. The major merger fraction exhibits an increase from $14.7 \pm 9.1\%$ at $z = 1$ to $26.6 \pm 8.4\%$ at $z = 3$, after which it remains approximately constant across the redshift range $3 < z < 6$. In contrast, the interaction fraction remains relatively stable across the range $2 < z < 5$. Our results indicate that late-stage major mergers are not the primary formation mechanism for SMGs at $z < 3$, while interactions appear to play a significant role across the broader redshift range of $1 < z < 6$. Additionally, HST-based major merger identifications may overestimate the true fraction by a factor of 1.7 at $z \sim 2$. These findings highlight the varying roles of mergers and interactions in driving the formation of massive, dusty star-forming galaxies across different redshifts.

Keywords: Galaxy morphology—Merger—Submillimeter Galaxies—Galaxy Classification–Ultra-luminous infrared galaxies

1. INTRODUCTION

Submillimeter galaxies (SMGs) represent a unique class of astronomical objects that have been extensively

Corresponding author: F. S. Liu and Nan Li
E-mail: fsliu@nao.cas.cn; nan.li@nao.cas.cn

observed at submillimeter and far-infrared wavelengths. They are characterized by high gas content (Tacconi et al. 2006; Riechers et al. 2010), high star formation rates (SFRs) (Barger et al. 2014), and active galactic nuclei (AGN) activity (Ueda et al. 2018). These galaxies indicate intense dusty starburst activity and significant mass assembly. Typically detected at high redshifts,

SMGs are considered the high-redshift counterparts of local ultra-luminous infrared galaxies (ULIRGs). They are ideal laboratories for investigating obscured star formation processes and chemical enrichment in the early universe.

Previous research has indicated a significant number of major merger events in SMGs at cosmic noon ($z \sim 2$). High-resolution imaging observations from the Hubble Space Telescope (HST) Advanced Camera for Surveys (ACS) suggest that the merger fraction exceeds 60% (Chapman et al. 2003; Conselice et al. 2003; Smail et al. 2004). Observations from the HST Wide Field Camera 3 (WFC3) F160W imaging indicate that the merger fraction in SMGs or ULIRGs is approximately 50% or higher (Kartaltepe et al. 2012; Chen et al. 2015; Stach et al. 2019). However, some studies have pointed out significant morphological differences in SMGs across rest-frame ultraviolet (UV) and optical wavelengths, suggesting that irregular morphologies may be more heavily influenced by dust obscuration rather than mergers (Swinbank et al. 2010). Additionally, numerical simulation studies have yielded divergent results. Some research suggests that a considerable fraction of SMGs are driven by intense starbursts triggered by mergers (Baugh et al. 2005; Narayanan et al. 2010; Hayward et al. 2013). In contrast, other studies, based on hydrodynamical simulations, propose that the observed properties of SMGs can be attributed to non-merging massive galaxies that maintain high star formation rates for approximately 1 billion years without deviating from the main sequence (Narayanan et al. 2015). This has raised questions about whether mergers are the primary driver of star formation in SMGs.

Due to the effects of dust extinction and star formation activity, the abundance of dust significantly influences the morphology of SMGs in the rest-frame optical band (Smail et al. 1999). In the early universe (i.e., at redshifts $z > 4$), these galaxies are almost invisible in HST observations (Smail et al. 1998; Enia et al. 2022). In contrast, the rest-frame near-infrared (NIR) band, less affected by dust extinction, predominantly reflects the radiation from old stellar populations. Studying SMGs' rest-frame NIR morphology and size can provide a clearer understanding of their stellar mass distribution, assembly processes, and formation scenarios.

With the release of James Webb Space Telescope (JWST) Near-Infrared Camera (NIRCam) data, further research on the properties of SMGs during the cosmic noon era ($1 < z < 3$) has emerged (Cheng et al. 2022, 2023; Boogaard et al. 2023; Gillman et al. 2023; Huang et al. 2023; McKinney et al. 2024). Notably, Cheng et al. (2023) studied 16 faint SMGs us-

ing the Atacama Large Millimeter/submillimeter Array (ALMA) and JWST/NIRCam data, revealing a diverse range of properties including both star-forming and quiescent galaxies. Most SMGs in their sample are compact disk galaxies, with a median half-mass radius of 1.6 kpc, showing little to no signs of disturbance. This suggests that secular growth could be a potential pathway for the assembly of high-mass disk galaxies. Additionally, JWST/MIRI data have been utilized to investigate the size and morphology of several high-redshift ($z \sim 4$) extreme dusty star-forming galaxies (DSFGs) (Smail et al. 2023; Crespo Gómez et al. 2024).

Recently, McKinney et al. (2024) conducted an in-depth analysis of 289 sub-millimeter galaxies (SMGs) in the COSMOS-Web field using the latest multi-band imaging data from the JWST. Their study revealed critical parameters such as galaxy mass, star-formation rate, and optical extinction. Notably, they found that approximately 30% of these galaxies had no previous optical/near-infrared detection records. Furthermore, their research indicated that about 17% of SMGs are undergoing major mergers. Gillman et al. (2024) utilized JWST/NIRCam and MIRI data to study the morphological and structural properties of 80 SMGs detected by ALMA within the redshift range of $1 < z < \sim 5$. The study found that approximately 60% of the SMGs appeared to be in late-stage major mergers or potential minor mergers, while about 40% displayed undisturbed disk-like morphologies. Additionally, the authors demonstrated that SMGs have comparable near-infrared sizes to less active galaxies but exhibit lower Sérsic indices. This suggests the presence of bulge-less disks with significant structured dust content, leading to distinct morphological characteristics. Despite these advances, there is still controversy regarding whether galaxy mergers play a decisive role in the evolution of SMGs at different redshifts and whether the sizes of SMGs evolve with redshift.

In this work, we construct a comprehensive sample of 222 SMGs with redshifts ranging from $1 < z < 6$ and dust luminosity $\log(L_{\mathrm{IR}}/L_{\odot}) > 12$. These SMGs were observed by the ALMA and the James Clerk Maxwell Telescope (JCMT) within the COSMOS and UDS fields. Utilizing the latest JWST/NIRCam and MIRI data, we conduct a detailed study of the effective radii in the rest-frame V-band and near-infrared (NIR) band of these SMGs, along with their merger fraction. This study traces their evolution from the cosmic dawn to the cosmic noon.

The paper is structured as follows: Section 2 describes the JWST/NIRCam and MIRI imaging data. Section 3 details the sample selection and the properties ob-

tained, leading to the main results and discussion in Sections 4 and 5. A brief summary is provided in Section 6. Throughout this study, we adopt a concordance cosmology with $H_0 = 70 \, \mathrm{km \, s^{-1} Mpc^{-1}}$, $\Omega_{\mathrm{m}} = 0.3$, and $\Omega_{\Lambda} = 0.7$.

2. DATA

2.1. *JWST imaging data*

We acquired raw broad-band JWST NIRCam imaging data for the COSMOS field, encompassing filters F090W to F444W, through programs 1727 (Kartaltepe et al. 2021), 1810 (Belli et al. 2021), 1837 (Dunlop et al. 2021), 1840 (Alvarez-Marquez et al. 2021), and 2514 (PI, Christina Williams). Similar data for the UDS field were obtained from programs 1837, 2514, and 3990 (Morishita et al. 2023). The raw MIRI imaging data in the COSMOS field, captured through filters F770W and F1800W, were sourced from programs 1727 and 1837. The raw MIRI data in the UDS field was derived from program 1837. Our analysis utilized JWST data collected in the COSMOS field before January 7, 2024, and data collected in the UDS field before January 21, 2024.

Our data reduction process began with uncalibrated data, applying Stage 1 of the JWST pipeline with standard parameters for initial detector corrections. We then addressed "snowball" artifacts, followed by Stage 2, where we subtracted "wisp" artifacts and reduced $1/f$ noise using the method described by Schlawin et al. (2020). Masks were applied to correct for persistence, dragon breath, ginkgo leaf, wisp features, and other artifacts. For Stage 3, we performed a custom astrometric correction and executed the `OutlierDetection` step. This was followed by a tailored outlier detection process and background subtraction before resampling. We initiated the World Coordinate System (WCS) calibration on JWST/F150W images, utilizing HST/F160W images from the CANDELS survey (Grogin et al. 2011; Koekemoer et al. 2011; Faber 2011). Subsequently, we extended this calibration process to other JWST bands, leveraging the JWST/F150W images as a reference. Mosaics were constructed for each observation, with a custom background subtraction applied to sub-mosaics to refine the final product.

The MIRI data underwent a similar pipeline process, incorporating super-sky flats in Stage 2 along with custom corrections for stripe and background effects. Stage 3 for MIRI followed a procedure analogous to that of NIRCam, with the primary difference being the reference catalog used for WCS alignment, which was sourced from F444W images.

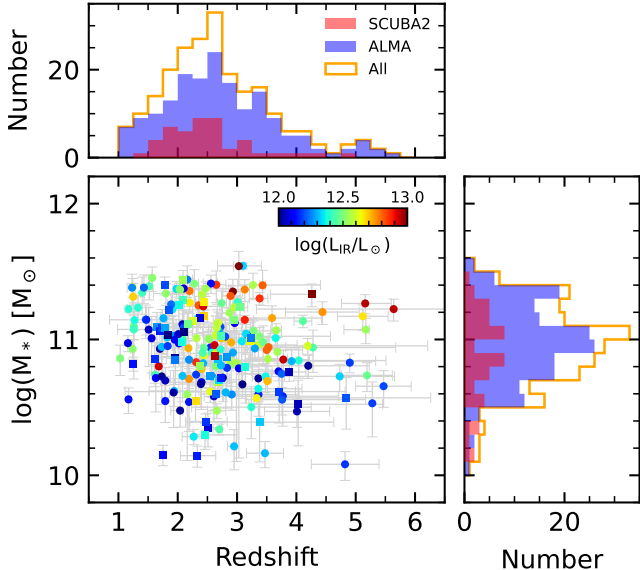The reduced NIRCam data covered 445 arcmin^2 in the COSMOS field and 273 arcmin^2 in the UDS field at F444W. The MIRI data spanned 259 arcmin^2 in the COSMOS field and 129 arcmin^2 in the UDS field at F770W, and all drizzled to a pixel scale of 0.″03. The empirical full width at half maximum (FWHM) of the point spread function (PSF) is 0.″165 at F444W and 0.″293 at F770W. This work is part of the Spatially Pixel-level Resolved Investigations into Nascent Galaxies with the James Webb Space Telescope (JWST-SPRING) project. This program aims to provide the astronomical community with extensive, homogeneous, and deep imaging data from JWST's NIRCam+MIRI, as well as spectroscopic data from NIRSpec and NIRCam/WFSS, all precisely matched with observations from the Hubble Space Telescope (HST). The JWST-SPRING dataset will encompass all previous deep extragalactic survey observations by HST, covering the five CANDELS fields – COSMOS, EGS, GOODS-North, GOODS-South, and UDS – as well as the broader COSMOS field and numerous smaller regions. For more information about the JWST-SPRING data, please visit the project website[1] and refer to the overview paper (Liu et al., in preparation).

2.2. *Submillimeter sources*

The SCUBA-2 COSMOS survey (S2COSMOS), conducted between 2016 and 2017, utilized the SCUBA-2 instrument at the JCMT to map the COSMOS field at $850 \, \mu\mathrm{m}$. As reported by Simpson et al. (2019), the survey delineated a 1.6 deg^2 MAIN region with a median noise level of 1.2 mJy beam^{-1} and a 1 deg^2 SUPP region with a sensitivity of 1.7 mJy beam^{-1}. The survey detected 1,020 and 127 submillimeter sources in the MAIN and SUPP regions, respectively, with a false detection rate of 2%, employing a PSF with a full width at half maximum (FWHM) of 14.″8.

The Automated Mining of the ALMA Archive in the COSMOS Field (A^{3}COSMOS) project, led by Liu et al. (2019), developed automated mining pipelines for the ALMA archive in the COSMOS field to enhance the usability of these data. By applying stringent selection criteria to ALMA detections, the project aimed to reduce the incidence of spurious sources, resulting in a catalog of ~ 700 galaxies within the redshift range $0.3 < z < 6$, with a minimal spurious fraction. The latest A^{3}COSMOS database comprises around 4,000 pipeline-processed continuum images from the public ALMA archive, yielding 2,050 unique detected sources, including those with and without a known optical counterpart (Adscheid et al. 2024).

---

[1] http://groups.bao.ac.cn/jwst_spring/

Figure 1. The stellar mass and redshift for the 222 SMGs. Data points are color-coded by dust luminosity. Squares represent JCMT-detected sources, while circles represent ALMA-detected sources. The top panel displays the redshift distribution, and the right panel shows the stellar mass distribution.

The AS2UDS catalog encompasses 716 single-dish submillimeter sources identified in the UKIDSS/UDS field through an $870\,\mu$m continuum survey with ALMA (Stach et al. 2019). The properties of these SMGs have been studied by Dudzevičiūtė et al. (2020).

3. SAMPLE SELECTION AND ANALYSES

3.1. *Sample Selection and Photometry*

We collected the S2COSMOS and A³COSMOS catalogs from the COSMOS field and the AS2UDS catalog from the UDS field. We then cross-matched all SMGs with sources observed by the JWST NIRCam and MIRI. For ALMA-observed sources, the resolution was sufficient to identify optical counterparts. Conversely, for JCMT/SCUBA-2 observed sources in the COSMOS field, we relied on the optical/near-infrared/radio counterparts identified by An et al. (2019) using a machine learning-assisted method (An et al. 2018). In total, we identified 453 submillimeter sources with observations in at least one JWST filter from both the COSMOS and UDS fields.

The integrated fluxes of SMGs in the HST bands (F814W, F105W, F125W, F140W, F160W) and JWST bands (F090W, F115W, F150W, F200W, F277W, F356W, F444W, F770W) were measured by accumulating the radial surface brightness profiles. These profiles were computed using the Python package `photutils` Bradley et al. (2024) on PSF-matched images with all

contaminations masked. We also cross-matched our sample with the COSMOS2015 catalog (Laigle et al. 2016) in the COSMOS field and multi-wavelength photometry data of SMGs in the UDS field (Michałowski et al. 2017; Dudzevičiūtė et al. 2020) to obtain additional far-IR data.

3.2. *Redshifts*

Initially, we utilized the `CIGALE` SED fitting code (Boquien et al. 2019; Yang et al. 2020, 2022) to estimate the photometric redshifts ($z_{\rm phot}$) of our SMG sample. Subsequently, we cross-matched our SMG sample in the COSMOS field with the publicly available spectroscopic redshift ($z_{\rm spec}$) and grism redshift ($z_{\rm grism}$) data of the COSMOS field (Kriek et al. 2015; Momcheva et al. 2016; Hasinger et al. 2018). Using the matched $z_{\rm spec}$, we assessed the precision of the $z_{\rm phot}$ from the `CIGALE` sample with more than five bands, resulting in a precision of $|\Delta z|/(1+z_{\rm spec}) = 0.09$. This precision is comparable to the $|\Delta z|/(1+z_{\rm spec}) = 0.12$ obtained by Uematsu et al. (2024a) and ~ 0.1 obtained by McKinney et al. (2024) using `CIGALE` for SED fitting of SMGs in the COSMOS field.

Concurrently, we cross-matched the SMG samples with the COSMOS-ReGEM catalog, in which the photoz is the median value of the COSMOS2020 CLASSIC catalog (Weaver et al. 2022), the COSMOS Photometric Redshifts with 30-Bands catalog (Ilbert et al. 2009), the UrtaVISTA catalog (Muzzin et al. 2013), and the COSMOS2015 catalog (Laigle et al. 2016) in the COSMOS field. A detailed description can be found in Ren et al. (2023). For our SMG sample, the ReGEM catalog provides a $z_{\rm phot}$ precision of approximately $|\Delta z|/(1+z_{\rm spec}) = 0.06$. Ultimately, in the COSMOS field, the priority for adopting the SMG best redshift ($z_{\rm best}$) is as follows: $z_{\rm spec}$ first, then the $z_{\rm phot}$ from ReGEM, and lastly the $z_{\rm phot}$ estimated by our `CIGALE`. Consequently, the $z_{\rm best}$ precision in the COSMOS field part is significantly better than $|\Delta z|/(1+z_{\rm spec}) = 0.09$.

For sources in the UDS field, we first used the best redshifts provided by the CANDELS catalog (Skelton et al. 2014; Momcheva et al. 2016), which mainly include $z_{\rm spec}$, $z_{\rm grism}$, and $z_{\rm phot}$. Then we considered the median of the three measurements: the $z_{\rm phot}$ with and without IR from Dudzevičiūtė et al. (2020), and our `CIGALE` $z_{\rm phot}$. Finally, we used our `CIGALE` $z_{\rm phot}$. We note that four SMGs in our sample in the UDS field were given JWST/NIRSpec spectra in Cooper et al. (2024), and we adopted the $z_{\rm spec}$ for these four SMGs.

3.3. *SED fitting*

In our analysis, we employed `CIGALE` to conduct SED fitting for our SMG sample, with photometric data span-

Table 1. Detection Counts of SMGs in HST and JWST Bands.

Field	F814W	F090W	F105W	F115W	F125W	F140W	F150W	F160W	F200W	F277W	F356W	F444W	F770W	Total
COS	117	65	18	156	90	62	154	103	75	162	74	154	99	163
UDS	34	53	5	56	35	24	57	36	56	59	59	59	26	59
All	151	118	23	212	125	86	211	139	131	221	133	213	125	222

ning from optical to submillimeter wavelengths. During the SED-fitting process, we utilized the `sfhdelayed` module. This module incorporated a main stellar population with ages ranging from 500 Myr to the age of the universe at the redshift of each SMG, and an e-folding time spanning from 100 to 10000 Myr. We adopted the `BC03` stellar population module (Bruzual & Charlot 2003), which was combined with a Chabrier initial mass function (IMF; Chabrier 2003). Dust attenuation was modeled using the `dust-modified-starburst` model (Calzetti et al. 2000), with $E(B-V)_{\mathrm{lines}}$ values ranging from 0.1 to 3. A factor of 0.44 was applied to $E(B-V)$ to correct for differential dust attenuation between old and young stellar populations (Calzetti et al. 2000; Charlot & Fall 2000; Wild et al. 2011). Dust emission was accounted for using the `Dale2014` prescription (Dale et al. 2014). Additionally, the `fritz2006` AGN module (Fritz et al. 2006) was incorporated into our SED fitting, allowing for an AGN fraction ranging from 0 to 0.5. This enabled us to account for the potential contribution of AGN activity to the overall SED. For additional details on the use of other modules and parameter settings in fitting SMG properties using `CIGALE`, one can refer to McKinney et al. (2024); Uematsu et al. (2024a,b).

Furthermore, a mock analysis was included in the fitting process to assess the reliability of our results. The dispersion between the SED results and the mock results was 0.09 dex for stellar mass (M_*) and 0.11 dex for L_{IR}, with no systematic bias observed. This indicates that our SED fitting method is robust and provides accurate estimates of the SMG properties.

3.4. *Final Sample*

Our final selection of SMGs is derived from a larger pool of 453 SMGs observed by JWST across two fields and is a carefully curated subset. The curation process is based on three principal criteria. First, we excluded sources with limited HST and JWST band coverage, as such constraints impede the precise determination of physical properties via SED fitting. Second, to define our sample selection boundary, we omitted sources with redshifts $z < 1$. Lastly, we filtered out sources that did not meet our thresholds for stellar mass and total infrared luminosity. These refinements have significantly enhanced the representativeness of our sample in terms of mass and infrared luminosity completeness. Our refined sample comprises 222 SMGs with stellar masses

greater than $\log(M_*/M_\odot) > 10$ and total infrared luminosities satisfying $12 < \log(L_{\mathrm{IR}}/L_\odot) < 13$, across the redshift range of $1 < z < 6$. In our sample, 46 SMGs overlap with those in Gillman et al. (2024).

Within this sample, 76 (34%) SMGs have spectroscopic or grism redshifts. The median stellar mass of our sample is $\log(M/M_\odot) = 10.97^{+0.29}_{-0.33}$, the median redshift is $z = 2.61^{+0.89}_{-0.82}$, and the median infrared luminosity is $\log(L_{\mathrm{IR}}/L_\odot) = 12.38^{+0.28}_{-0.24}$. The distribution of stellar masses and redshifts, along with the infrared luminosities of our sample, is depicted in Figure 1. Table 1 shows the number of our final samples detected in the JWST and HST filters. The mean filters used for SED fitting of our SMGs are 12 filters spanning from the optical to ALMA band 3. In our sample, the detections from mid-infrared to far-infrared are as follows: 99 (45%) at MIPS 24 μm, 22 (10%) at 100 μm, 30 (14%) at 160 μm, 88 (40%) at 250 μm, 78 (35%) at 350 μm, and 42 (19%) at 500 μm.

We present a comparison of the SMG properties derived from our `CIGALE`-based SED fitting with those from previously published SMG catalogs. The stellar masses derived from `MAGPHYS` (Da Cunha et al. 2008) are larger than our results by 0.1-0.2 dex in the A³COSMOS (Adscheid et al. 2024) and the AS2UDS catalog (Dudzevičiūtė et al. 2020). Uematsu et al. (2024a) found that the stellar mass derived from `CIGALE` is 0.3-0.4 dex lower than that derived from `MAGPHYS` due to the different dust attenuation models adopted in SED fitting. A similar difference is observed in the H-band mass-to-light ratio recovered by `CIGALE`, which is ~0.2 dex less than the average among ALESS SMGs derived from `MAGPHYS` in McKinney et al. (2024). Considering a deviation of ~ 0.2 dex, our median stellar mass is consistent with the median stellar masses provided by A³COSMOS (Adscheid et al. 2024), SCUBADive (McKinney et al. 2024), and AS2UDS (Dudzevičiūtė et al. 2020). The L_{IR} shows systematic deviations of 0.04 dex between our results and A³COSMOS (Adscheid et al. 2024) and AS2UDS (Dudzevičiūtė et al. 2020). Since our stellar mass is primarily used to select SMGs with $\log(M_*/M_\odot) > 10$, and SMGs with $\log(M_*/M_\odot) < 10.5$ actually make up a very small fraction of our sample, as shown in Figure 1, even considering an underestimation of ~ 0.2 dex in stellar mass compared to previous work,

a new selection criterion of $\log(M_*/M_\odot) > 9.8$ would not significantly affect our sample.

Among our 222 SMGs, 163 are in the COSMOS field, with 48 from the S2COSMOS survey (Simpson et al. 2019) based on JCMT/SCUBA-2 observations and the remaining 115 from the A³COSMOS catalog (Liu et al. 2019; Adscheid et al. 2024) based on ALMA observations. In the UDS field, there are 59 SMGs, all from the AS2UDS survey (Stach et al. 2019) based on ALMA observations. The optical and near-infrared counterparts of the 48 S2COSMOS sources were identified by An et al. (2019) using a machine learning method with an accuracy exceeding 85%. This implies that fewer than 8 uncertain samples exist among these 48 sources. The remaining sources, which are based on ALMA observations, are more reliable. Therefore, the uncertainty of SMGs in our final sample is considerably less than 4%.

3.5. *Size measurements*

Our objective is to examine the size evolution of these SMGs separately in the rest-frame V-band and rest-frame NIR-band. To accomplish this, we selected the rest-frame V and NIR-bands using the rest-frame wavelengths corresponding to the F115W to F770W bands at different redshifts. Specifically, we chose the JWST band closest to $0.5\,\mu m$ within the 0.4–$0.6\,\mu m$ range to represent the rest-frame V-band, and the band closest to $1.6\,\mu m$ (H-band) within the 1–$2\,\mu m$ range to represent the rest-frame NIR-band. For example, for an SMG at $z = 1.85$, the rest-frame 0.4–$0.6\,\mu m$ includes the F115W and F150W bands, but the rest-frame wavelength of F150W is closest to $0.5\,\mu m$. Meanwhile, the rest-frame 1–$2\,\mu m$ range encompasses the F356W and F444W bands, with the rest-frame wavelength of F444W being closer to $1.6\,\mu m$. Consequently, for this SMG, the rest-frame V-band is F150W, and the rest-frame NIR-band is F444W.

We utilized four separate Sérsic fitting packages—`PetroFit` (Geda et al. 2022), `Pysersic` (Pasha & Miller 2023), `GALFIT` (Peng et al. 2002), and `Statmorph` (Rodriguez-Gomez et al. 2019)—to perform independent Sérsic fittings. As a result, the Sérsic index (n) and effective radius (R_e) for the rest-frame V and NIR-band of each SMG were measured using these four tools on the contaminations-masked images. By comparing the fitting results from different software, we found that the systematic bias in the fitted R_e values obtained from different software is as small as $0.''01$ in the rest-frame V-band and $0.''004$ in the rest-frame NIR-band. Among them, the fitting results from `PetroFit` exhibit fewer outliers compared to other software. Therefore, if the fitting result from `PetroFit` lies between the results of

Table 2. Number of SMGs used in the size evolution fitting.

Range	R_e (V) (kpc)	N_V	R_e (NIR) (kpc)	N_{NIR}
$1 < z < 2$	$4.82^{+1.72}_{-2.27}$	47 (92%)	$2.93^{+1.71}_{-0.99}$	46 (90%)
$2 < z < 3$	$3.64^{+1.84}_{-1.18}$	83 (80%)	$2.22^{+1.51}_{-0.76}$	93 (89%)
$3 < z < 4$	$2.61^{+1.71}_{-0.63}$	33 (70%)	$1.66^{+1.48}_{-0.54}$	35 (74%)
$4 < z < 5$	$2.57^{+0.75}_{-0.42}$	10 (77%)	$1.73^{+0.74}_{-0.41}$	8 (62%)
$5 < z < 6$	$2.21^{+1.29}_{-1.22}$	6 (86%)	$1.24^{+1.86}_{-0.43}$	4 (57%)

the other three softwares, we adopt the `PetroFit` result. If `PetroFit` does not provide a fitting value or its result falls outside the range of the other three software results, we then use the median value from the remaining three softwares. This approach effectively reduces the impact of outliers that can arise from relying on a single fitting software.
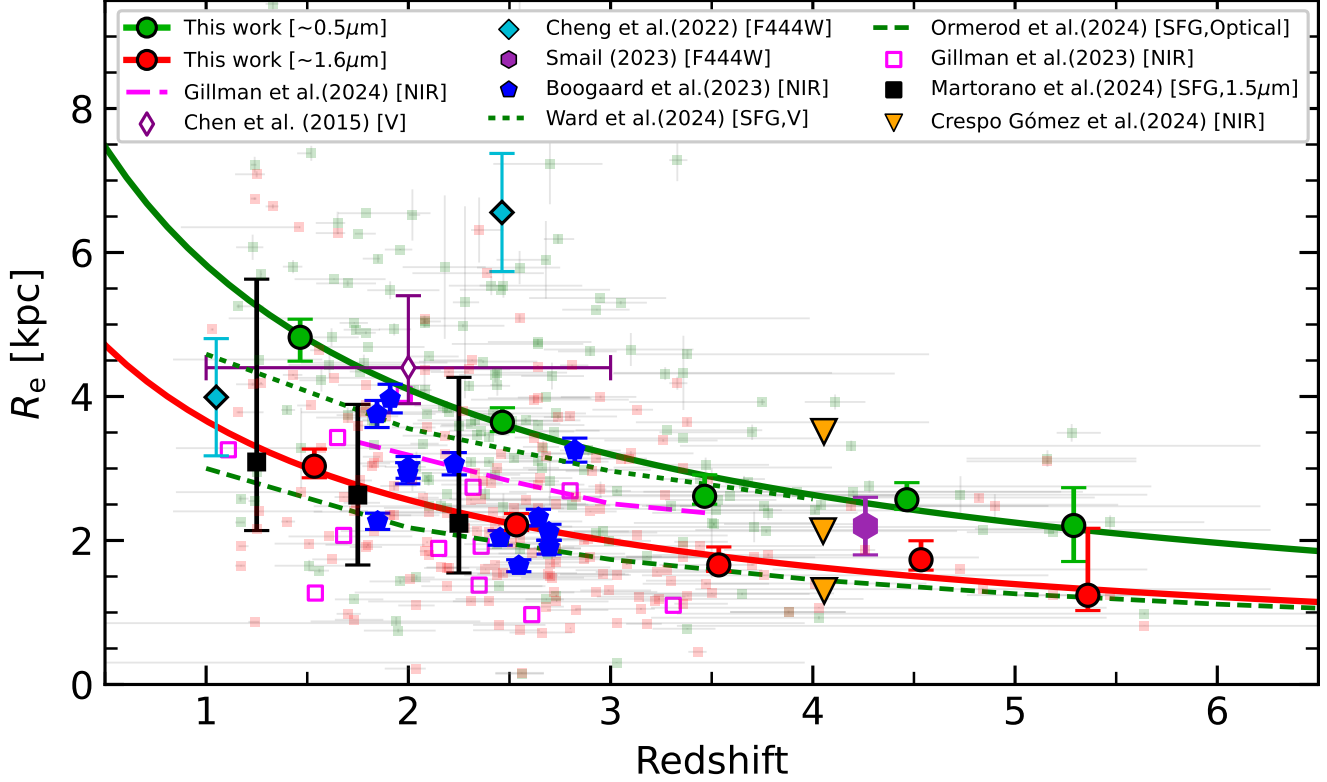
There are 179 (80%) sources with measured R_e in the V-band, with a median R_e and 16th to 84th percentile intervals of $3.60^{+2.19}_{-1.44}\,kpc$. In the NIR-band, there are 186 (81%) sources with measured R_e, with a median R_e and 16th to 84th percentile intervals of $2.26^{+1.53}_{-0.99}\,kpc$. There are 158 SMGs (68%) having both V-band and NIR-band size measurements.

4. RESULTS

4.1. *Size evolution*

We performed a detailed analysis to examine the relationship between the effective radius (R_e) of SMGs in both the rest-frame V-band ($\sim 0.5\,\mu m$) and rest-frame NIR-band ($\sim 1.6\,\mu m$) and redshift, as shown in Figure 2. The median size, as well as the 16th to 84th percentile intervals, the number, and fraction with size measurements in each redshift bin are provided in Table 2. Our results indicate that in the V-band, the average effective radius (R_e) of SMGs significantly increases, from $2\,kpc$ at $z = 6$ to $5.5\,kpc$ at $z = 1$. A similar trend is observed in the NIR band, where R_e increases from $\sim 1.3\,kpc$ to $\sim 3.5\,kpc$ within the same redshift interval. This suggests that the spatial distribution of star formation activity within SMGs is more extended at lower redshifts, indicating that the stellar mass may be more centrally concentrated than in unobscured star-forming regions.

By fitting the $R_e - z$ relationship, we find that the power-law function exhibits smaller AIC and BIC values, as well as a smaller chi-square value, compared to other simple functional forms such as linear functions. This suggests that the power-law model is better suited to describe the evolution of SMG size with redshift. The derived $R_e - z$ relations are as follows: in the V-band, $R_e = (10.62 \pm 1.03) \times (1+z)^{-0.87 \pm 0.08}$; in the NIR-band,

Figure 2. Effective Radius as a Function of Redshift for Our SMGs. The green circles denote the median R_e of our SMGs in the rest-frame V-band, while the red circles represent the median R_e of our SMGs in the rest-frame NIR-band for each redshift bin. The X-axis positions of the red and green circles are shifted by ± 0.03 for clarity. The solid green and red lines represent the best-fitting R_e evolution with redshift for our sample in the rest-frame V-band and NIR-band, respectively. The error bars on our green and red data points represent the uncertainties of the median value in each redshift bin. The magenta dashed line traces the NIR ($\sim 1\mu m$) size evolution of luminous ALMA-detected SMGs in the COSMOS and UDS fields, as measured with JWST/NIRCam and MIRI by Gillman et al. (2024). The green dotted line delineates the rest-frame optical size evolution of star-forming galaxies for $\log(M_*/M_\odot) > 10.5$ at $0.5 < z < 5$, while the green dashed line shows the size evolution for $\log(M_*/M_\odot) > 9.5$ at $0.5 < z < 8$, both from the JWST/CEERS survey by Ward et al. (2024) and Ormerod et al. (2024), respectively. Cyan markers represent SMGs in the SMACS J0723.3–7327 field, with sizes derived from JWST/F444W by Cheng et al. (2022). Unfilled magenta squares represent SCUBA-2 SMGs selected within the JWST/CEERS survey by Gillman et al. (2023). Purple hexagons highlight an SMG with $\log(M_*/M_\odot) \sim 11.8$ at $z = 4.26$ in the Prime Extragalactic Areas for Reionization and Lensing Science (PEARLS) field, with size derived from JWST/NIRcam F444W by Smail et al. (2023). Blue pentagons correspond to SMGs with $\log(M_*/M_\odot) > 10$ and redshifts between $1.8 < z < 4.6$ in the Hubble Ultra Deep Field (HUDF), with sizes determined from JWST/MIRI F560W by Boogaard et al. (2023). Orange triangles represent three SMGs with very high IR luminosities ($L_{IR} > 10^{13}$ L$_\odot$), with sizes determined from JWST/MIRI F560W by Crespo Gómez et al. (2024). The unfilled purple diamonds represent the rest-frame V size at $z \sim 2$ given by Chen et al. (2015) using HST/F160W data. The black squares indicate the median size of massive star-forming galaxies ($11 < \log(M_*/M_\odot) < 11.5$) at rest-frame $1.5\,\mu m$, measured by Martorano et al. (2024) for the redshift range of $0.5 < z < 2.5$.
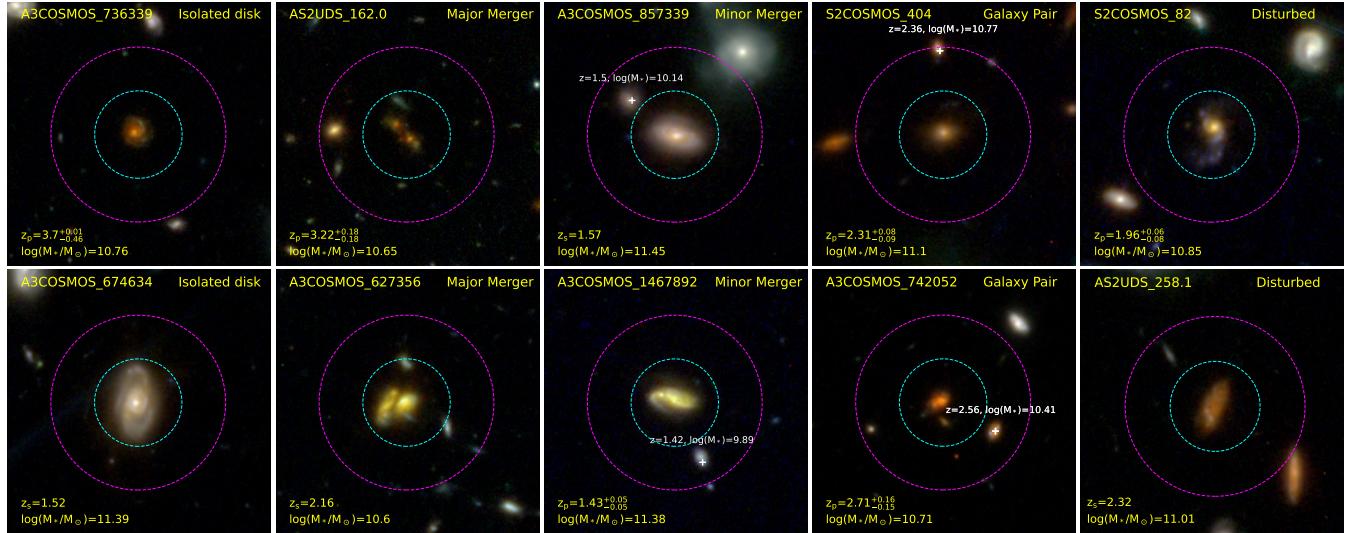
$R_e = (6.74 \pm 0.93) \times (1+z)^{-0.88 \pm 0.11}$. These relations provide a quantitative framework for understanding the cosmic evolution of sizes in SMGs.

Additionally, we find that the rest-frame NIR sizes of SMGs in previous studies based on JWST observations generally align with the evolutionary trend we observed at $z < 4$. However, several recent studies (Smail et al. 2023; Crespo Gómez et al. 2024; Gillman et al. 2024) indicate that the average sizes of massive SMGs are larger than those of the SMGs we studied. This discrepancy may be due to differences in sample selection and rest-frame band selection.

4.2. Merger fraction evolution

In our analysis of the merger fraction, we initially identified galaxies with distinct merger signatures, such as double nuclei, multicomponent structures, or companion galaxies within 15 kpc exhibiting tidal disturbances. These features indicate that the galaxies are in the late stages of major mergers. JR and FL independently identified major mergers for this SMG sample. If an SMG

Figure 3. Example images of SMGs classified by visual identification. The radius of cyan and magenta circle are 15 kpc and 30 kpc respectively.
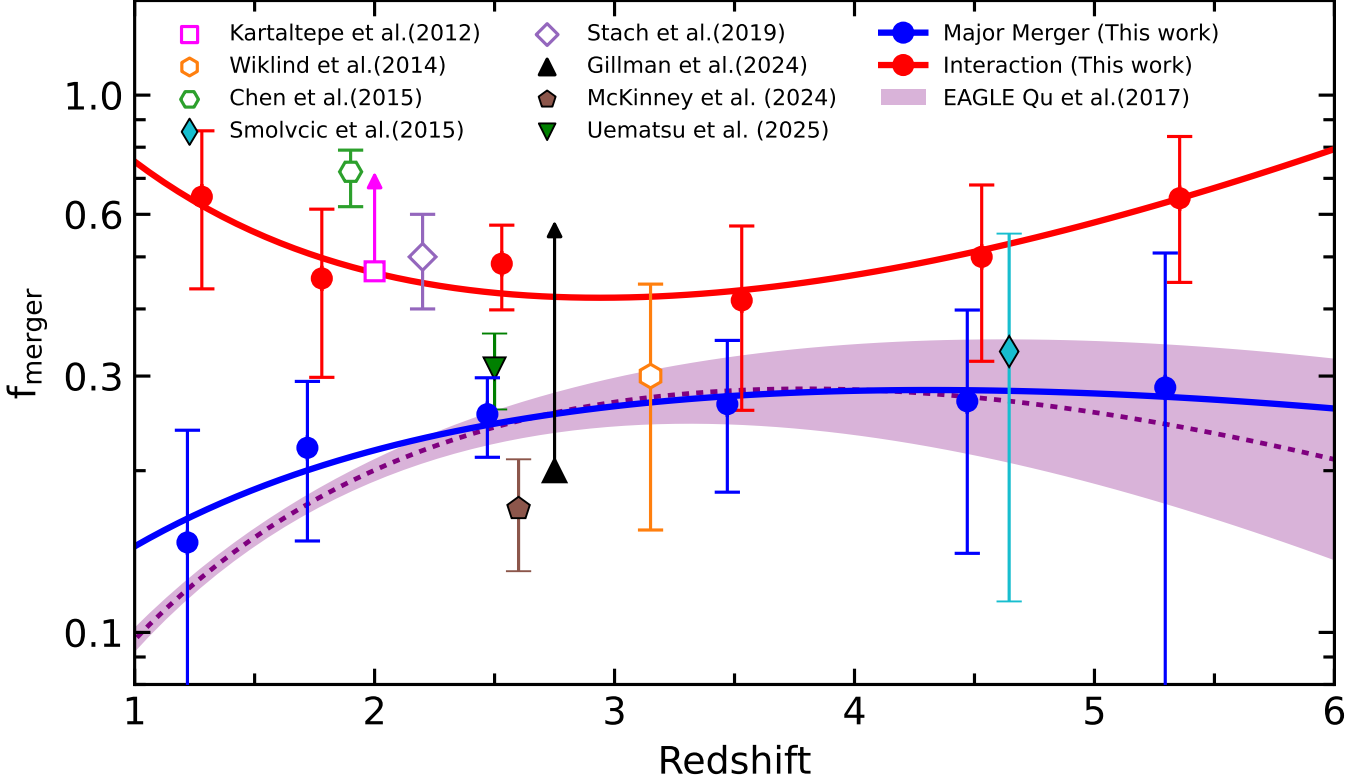
was identified as a major merging galaxy by both individuals, it was marked as a 'reliable' major merger. If an SMG was considered a merger by only one of us, it was marked as a 'tentative' major merger. We identified 49 SMGs as 'reliable' major mergers and an additional 10 SMGs as 'tentative' major mergers. This classification establishes a major merger fraction of $24.3 \pm 3.7\%$ in our sample. This result is consistent with recent identifications of the major merger fraction in the COSMOS and UDS fields (McKinney et al. 2024; Gillman et al. 2024; Uematsu et al. 2024b) using JWST data. It is important to note that visual identification is a reliable method for detecting galaxies in the late stages of major mergers. However, we acknowledge that this approach may overlook galaxies in the early stages of merging or those that have already completed the process. Therefore, the merger fraction we report can be considered a conservative estimate.

Furthermore, we identified potential galaxy pairs. For SMGs with companion galaxies within 30 kpc, we first cross-matched the COSMOS2020 catalog and CANDELS catalogs. If the companion galaxies were cross-matched and had spectroscopic or photometric redshifts, we used the galaxy pair selection method to identify mergers. Specifically, if both the SMG and the companion galaxy have spectroscopic redshifts, their relative velocity $|\Delta V| < 500$ km/s is considered a galaxy pair. When one has a spectroscopic redshift and the other has a photometric redshift, $|\Delta z|$ less than the photometric redshift error σ_z is considered a galaxy pair. When both galaxies have photometric redshifts, $|\Delta z| < \sqrt{\sigma_1^2 + \sigma_2^2}$ is considered a galaxy pair. An SMG is considered a merger and marked as 'reliable' if it has at least one companion galaxy within 30 kpc that meets the aforementioned criteria. If an SMG has companion galaxies within 30 kpc but no previous redshift measurements, it is marked as 'tentative'. We also identified galaxies with disturbed morphologies and potential minor mergers based on the presence of distinct clumps at the peripheries of SMGs or irregular dwarf galaxies affected by tidal forces within a 30 kpc radius. The identification method is similar to that for major mergers. Our sample includes 84 interactions marked as 'reliable', and 47 interactions marked as 'tentative'. This suggests that $48.4 \pm 11.1\%$ of SMGs may be involved in interactions.

Figure 4 illustrates the evolution of the merger fraction with redshift, accompanied by a compilation of existing data on SMGs or ULIRGs. The figure shows that the fraction of late-stage major mergers is consistent with the predictions of the EAGLE simulation. Our major merger fraction shows a significant increase from $14.7\pm9.1\%$ at $z = 1$ to $26.6\pm8.4\%$ at $z = 3$, and after which it stabilizes and remains approximately constant across the redshift range $3 < z < 6$. We find that the interaction fraction remains relatively stable across the range $2 < z < 5$.

We provide the best-fit relationships between the merger fraction (f_{mer}) and redshift for two types of mergers. The merger galaxy fraction as a function of redshift is modeled according to the form presented by Conselice et al. (2009), which is widely adopted in studies examining the evolution of merger fractions or merger rates with redshift. The derived $f_{\mathrm{mer}} - z$ relations are as follows: for late-stage major mergers (represented by the blue solid line in Figure 4), $f_{\mathrm{mer}} = (0.08 \pm 0.02)(1 + z)^{(1.90\pm0.71)} \exp\left[-(0.36 \pm 0.17)(1 + z)\right]$; for interactions

Figure 4. Merger Fraction as a Function of Redshift for Our SMGs. The blue and red points represent the fractions of late-stage major mergers and interactions, respectively, within different redshift bins of our sample. Error bars represent the errors of merger identification and statistical errors. The solid blue and red lines represent the best-fit trends for the evolution of these merger fractions with redshift. The dashed purple lines show the merger fraction evolution for massive ($\log(M_*/M_\odot) > 10$) normal galaxies in the EAGLE simulation (Qu et al. 2017). The open magenta squares correspond to the merger fraction of far-infrared selected ULIRGs at $z \sim 2$ (Kartaltepe et al. 2012). The open orange hexagon represents the ongoing mergers among ten SMGs in the GOODS-S field, as detailed by Wiklind et al. (2014). The open green hexagon denotes ALMA-detected SMGs identified by Chen et al. (2015) in the ECDFS field. The cyan diamond signifies two mergers among six $z > 4$ SMGs in the COSMOS field, as reported by Smolčić et al. (2015). The open purple rhombi indicate the merger fraction of ALMA-detected SMGs in the UKIDSS/UDS field at $z = 2.2 \pm 0.1$, according to Stach et al. (2019). The black triangle depicts the lower limits of the merger fraction for ALMA-detected SMGs from the AS2COSMOS and AS2UDS surveys, as compiled by Gillman et al. (2024). The brown pentagon represents the merger fraction of SMGs identified by McKinney et al. (2024) in the COSMOS-Web field. The green triangle represents the merger fraction identified by Uematsu et al. (2024b) in the COSMOS field. Unfilled markers represent mergers identified from HST/F160W imaging, while filled markers correspond to those identified through JWST and ALMA imaging.
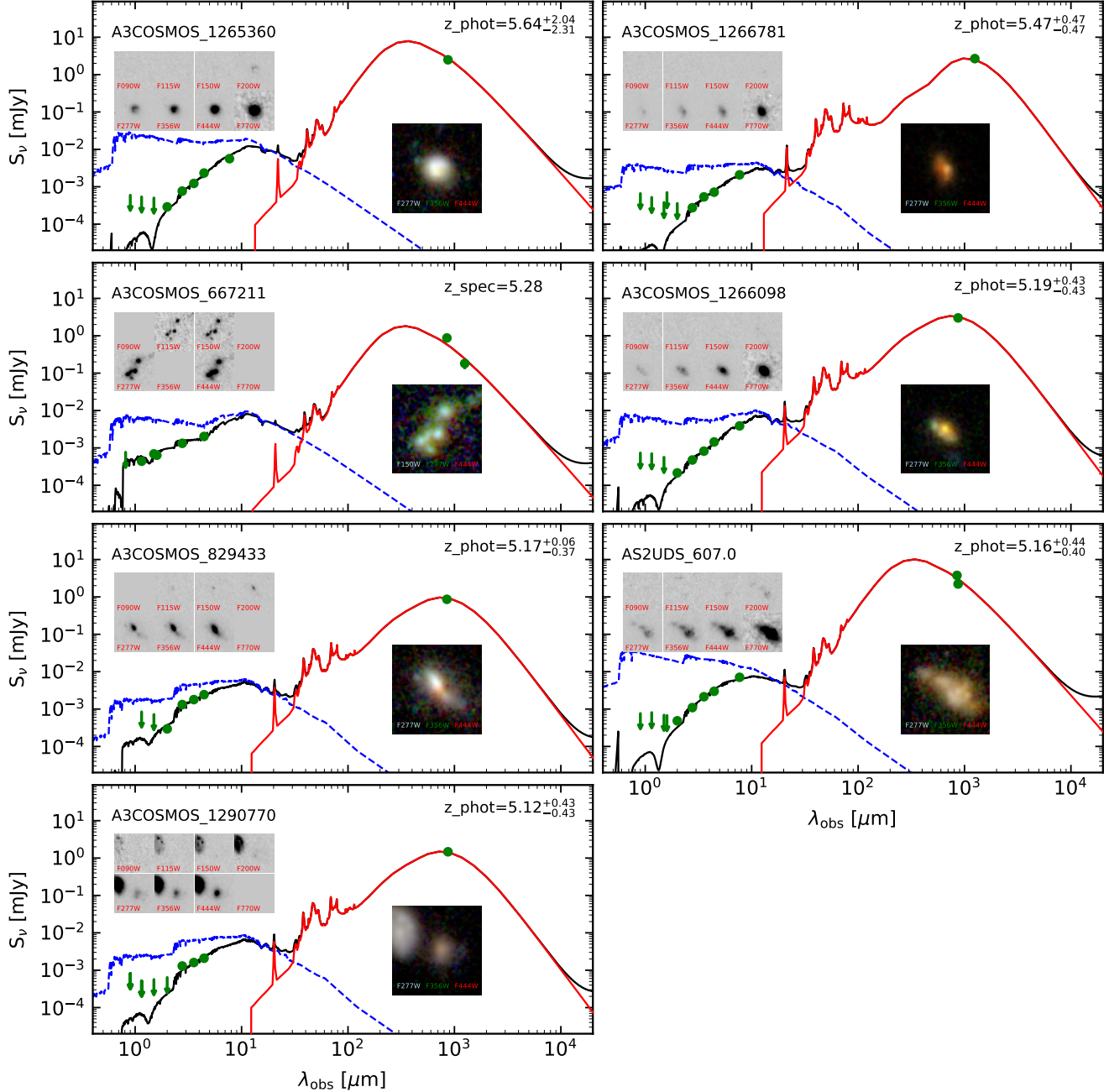
(represented by the red solid line in Figure 4), $f_{\mathrm{mer}} = (1.35 \pm 0.31)(1 + z)^{(-3.15 \pm 0.69)} \exp\left[(0.80 \pm 0.17)(1 + z)\right]$.

We emphasize that employing a constant merger fraction offers statistically robust constraints for elucidating the role of mergers in the evolution of SMGs. The evolutionary trends presented in this work should be interpreted as qualitative indicators of merger fraction evolution, rather than definitive quantitative relationships. As demonstrated in Figure 4, each data point is associated with considerable uncertainties, predominantly stemming from the restricted sample size and systematic limitations inherent in merger identification through visual morphological classification. This observational constraint implies that the current data quality does not

warrant the implementation of more sophisticated evolutionary parameterizations, as such approaches would likely introduce substantial risks of overfitting.

4.3. Morphology of $z > 5$ SMGs

We conducted a detailed morphological analysis of seven SMGs with redshifts $z > 5$ in our sample. Figure 5 displays their best-fit Spectral Energy Distributions (SEDs) and multi-band images. Among these seven SMGs, only A3COSMOS_667211 exhibits multiple components, indicating that it is in a late stage of a major merger. A3COSMOS_829433 and AS2UDS_607.0 display structures resembling tidal tails, suggesting that they may have undergone major merg-

Figure 5. Multi-band JWST/NIRCam and MIRI Images and Best-fit SEDs of 7 SMGs with Redshifts $z > 5$. The ID and redshift of each SMG are indicated in the upper left corner of the bottom panels. Where available, the effective radius and Sérsic index n for each band are presented in the upper left corner of the respective images. In each image, the physical size corresponding to the side length is 15 kpc.

ers. A3COSMOS_1266098 has blue clumps in its outskirts, which may indicate a minor merger, with the outer clumps representing recently accreted dwarf galaxies with high star formation rates and low dust content. A3COSMOS_1266781 shows a disturbed morphology. In addition, the remaining two, A3COSMOS_1265360 and A3COSMOS_1290770, display undisturbed disk-like structures. Thus, among the seven SMGs with redshifts

$z > 5$, most show signs of mergers or interactions, implying that the majority of SMGs in the early universe were likely formed through mergers or interactions.

5. DISCUSSIONS

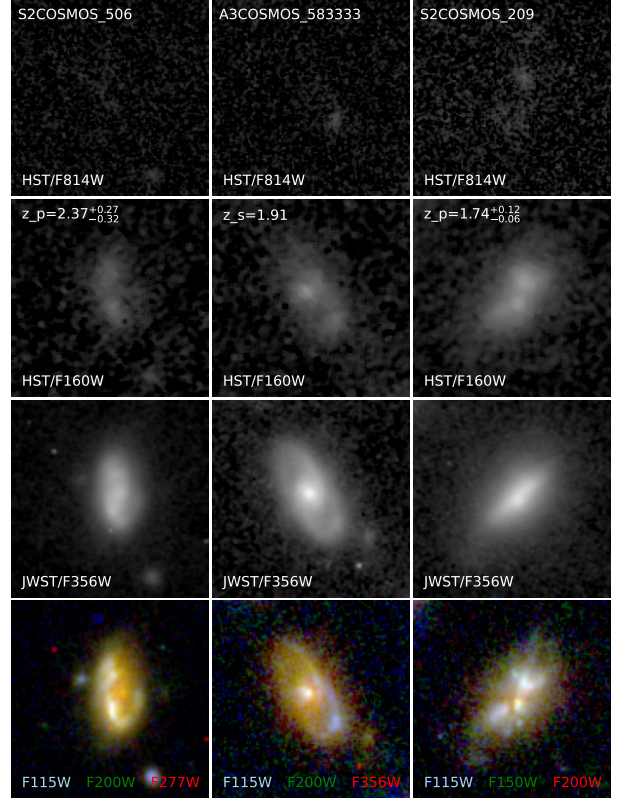### 5.1. *Impact of Cosmic Dimming effect on Merger Identification*

The cosmic dimming effect, which follows the form $(1 + z)^{-4}$, significantly impacts the detection and classification of galaxies at higher redshifts. For late-stage mergers in our sample, characterized by multi-component structures and strong tidal features, the cosmic dimming effect has a relatively minor impact on their identification. This is because these galaxies have higher surface brightness and more pronounced structural features that are less affected by the dimming effect. However, for minor mergers, the cosmic dimming effect can lead to an underestimation of their fractions as redshifts increase. For galaxy pairs, our SMG sample has a median stellar mass of $\log(M_*/M_\odot) \sim 10^{11}$. Even considering that the companion galaxies have a mass one order of magnitude lower ($\log(M_*/M_\odot) \sim 10^{10}$), the depth of the JWST multi-band imaging is sufficient to detect these galaxy pairs without significantly affecting their estimation. Regarding disturbed morphologies at $z > 4$, only two galaxies in our sample were identified as having disturbed morphologies, contributing only 10% to the total in this redshift range. Even considering a potential overestimation of this 10%, it does not affect the increasing trend of interactions in the $4 < z < 6$ range. Additionally, considering the underestimation of minor mergers at higher redshifts, the increasing trend of the interaction fraction in the $4 < z < 6$ range is even more pronounced.

In conclusion, the cosmic dimming effect and detection limits have a limited impact on our estimates of the major merger fraction. Although there is an underestimation of the interaction fraction at higher redshifts, it does not affect the overall increasing trend. This suggests that our results are robust and provide a reliable understanding of the evolution of merging and interacting galaxies across the redshift range studied.

5.2. Compare the R_e with previous works

As illustrated in Figure 2, the effective radii (R_e) of our SMGs at redshifts $z \sim 2$ are generally consistent with most previous research on the sizes of SMGs, such as the findings by Boogaard et al. (2023) and Gillman et al. (2023, 2024). However, as redshift increases, some previous studies, particularly the research by Gillman et al. (2024, hereafter G24), begin to deviate from our measurement results.

We find that the size-redshift evolution relationship in G24 lies between our rest-frame V and rest-frame NIR-bands. We attribute this primarily to the fact that G24's R_e is around 1 μm, while our V-band is close to 0.5 μm and our NIR is close to 1.6 μm. In addition, even after accounting for a 0.2 dex underestimation in our stellar mass, G24's median stellar mass is still 0.1 dex higher

Figure 6. **The HST/F814W and F160W images, as well as longer-wavelength JWST/NIRCam images and pseudo-color images of six typical disk-dominated SMGs at** $z \sim 2$**.** The ID and redshift of each galaxy are indicated in the upper left corner of the bottom panels. In each image, the physical size of the side length is 30 kpc.

than our sample. In fact, after considering both the band and stellar mass, the size-mass relation is consistent with our results. A comparison of our size-mass relation with the results of G24 is provided in Appendix B.

Additionally, we compared the effective radii of SMGs in the rest-frame V-band with those of the general star-forming galaxies (SFGs) recently observed by the JWST. We found that within the redshift range of $1 < z < 5$, the R_e of SMGs in the rest-frame V-band is approximately 1–2 kpc larger than that of SFGs. This is likely because SMGs typically possess a greater stellar mass and more extensive star formation activity than normal SFGs, and therefore, they have larger effective radii. In the rest-frame near-infrared band, the evolution of our SMG size ($\sim$1.6 μm) with redshift is consistent with the size (~ 1.5 μm) evolution of massive SFGs provided by Martorano et al. (2024) in the redshift range of $1 < z < 2.5$.

5.3. *Previous overestimate of merger fraction at $z \sim 2$*

We observe that the merger fractions of SMGs or ULIRGs at redshift $z \sim 2$, as previously determined from HST WFC3/F160W images (Kartaltepe et al. 2012; Chen et al. 2015; Stach et al. 2019), reach upper limits of our "interaction" fraction. We hypothesize that at redshift $z \sim 2$, the HST/F160W band roughly corresponds to the rest-frame V-band, and the merger-like morphological features exhibited by a substantial number of galaxies may be substructures within the galaxies. These substructures could be misidentified as mergers, resulting in an overestimation of the merger fraction.

To evaluate the potential overestimation of the merger fraction based solely on HST observational images, we analyzed 58 sources within our sample of SMGs in the redshift range of $1.5 < z < 2.5$ that have HST/F160W observations. We identified 22 ± 2 major mergers using the HST/F160W images, which account for approximately a major merger fraction of $37.9\pm3.4\%$. However, by employing multi-band images from JWST, we identified only 13 ± 1 major mergers, representing a fraction of $22.4\pm5.7\%$. This suggests that the merger fraction obtained previously using HST may overestimate the true major merger fraction by 69.2%. Although a considerable fraction of the "interactions" category may not be mergers in our identification, the fraction obtained from HST/F160W images is $55.2\pm5.2\%$. In contrast, the result obtained from JWST images is $46.6\pm10.8\%$, indicating an overestimation of nearly 18.5%. Figure 6 presents the HST/F814W and F160W images, as well as longer-wavelength JWST/NIRCam images and pseudo-color images of three typical disk-dominated SMGs at $z \sim 2$.

5.4. *Formation Mechanisms of SMGs*

Our study conducted a detailed investigation of the merger fraction of SMGs across a broad redshift range of $z = 1-6$, with particular focus on the early cosmic epoch at redshift $z > 5$, when the age of the universe was less than two billion years. During this period, the impact of late-stage major merger events on SMG formation might have been less significant.

Upon comparison with previous studies, we find that our major merger fraction aligns well with the latest merger fractions obtained using JWST/NIRCam confirmations, which are approximately 20% (Gillman et al. 2024; McKinney et al. 2024; Uematsu et al. 2024b). This fraction is also consistent with the major merger fraction of normal galaxies provided by the EAGLE simulations (Qu et al. 2017), suggesting that major mergers may not be the dominant mechanism for the starburst phase in SMGs.

In addition to our main findings, we observe that the fraction of interacting galaxies within SMGs remains relatively constant in the redshift range $2 < z < 5$. This period coincides with a rapid increase in the cosmic star formation rate density (Madau & Dickinson 2014). The overall star-forming activity in galaxies is intense, allowing a greater number of normal massive disk galaxies to maintain high levels of star formation activity. This activity heats the dust, leading to the formation of submillimeter galaxies (SMGs). In contrast, at higher redshifts ($z > 5$) or lower redshifts ($z < 2$), interactions are necessary to sustain high levels of star formation activity in massive galaxies, which in turn heats the dust. Particularly at lower redshifts, massive galaxies have largely shut down star formation and can only briefly maintain high star formation activity through the merger of a gas-rich galaxy (wet merger).

We find that a substantial fraction of disk SMGs exhibit blue clumps and arcs at cosmic noon. Some SMGs exhibit PSF-like morphologies, implying that they likely have AGN activity. Therefore, we posit that the formation mechanisms of SMGs are primarily consistent with those that sustain high levels of star-forming activity. The intense star formation activity in SMGs can be triggered by instabilities and fragmentation within the gas disk, as well as by mergers and interactions. Additionally, AGN activity contributes to a small fraction of SMGs. However, mergers and interactions not only trigger star formation but also AGN activity. For instance, Uematsu et al. (2024b) observed that approximately 47% of AGNs in SMGs are triggered by major mergers. Consequently, the fraction of SMG formation mechanisms attributed to AGN activity is likely to be half of what is observed in the AGN fraction within SMGs.

6. SUMMARY

In this study, we investigate the evolution of size and merger fraction for a sample of 222 SMGs with dust luminosity of $12 < \log(L_{IR}/L_\odot) < 13$. These SMGs were identified through ALMA and JCMT, and their properties were studied using the advanced imaging capabilities of JWST/NIRCam and MIRI across a broad redshift range of $1 < z \lesssim 6$. Our sample has a median redshift of $z = 2.61^{+0.89}_{-0.82}$ and a median stellar mass of $\log(M_*/M_\odot) = 10.97^{+0.29}_{-0.33}$. Our key findings are as follows:

1. We observe a significant decrease in the effective radius (R_e) of SMGs with increasing redshift in both the rest-frame V-band and NIR band. The R_e of SMGs follows $R_e \propto (1+z)^{-0.87\pm0.08}$ in the rest-frame V-band and $R_e \propto (1+z)^{-0.88\pm0.11}$ in

the NIR band. The NIR-band size evolution of our SMGs resembles that of massive star-forming galaxies at lower redshifts ($1 < z < 2.5$).

2. Our analysis reveals a major merger fraction of $24.3 \pm 3.7\%$ and an interaction fraction of $48.4 \pm 11.1\%$ within the sample. The major merger fraction exhibits a significant redshift dependence, showing a gradual increase at $z < 3$ before reaching a plateau at $3 < z < 6$. In contrast, the interaction fraction, which encompasses both major and minor mergers, potential pairs, and galaxies with disturbed morphologies, maintains a relatively constant value across the redshift range of $2 < z < 5$.

3. Among the seven SMGs with $z > 5$ in our sample, most exhibit merger or interaction signatures, with only a few showing undisturbed disk-like structures. This implies that the majority of SMGs in the early universe were likely formed through mergers or interactions.

4. HST-based studies may overestimate the major merger fraction by a factor of ~ 1.7 at $z \sim 2$. Our analysis using multi-band JWST images suggests that the true merger fraction is lower than previously thought, highlighting the importance of high-resolution, multi-wavelength data in accurately identifying merging systems.

These findings provide valuable insights into the formation and evolution of SMGs across cosmic time, emphasizing the complex interplay between mergers, interactions, and internal processes in driving their observed properties. Our results suggest that late-stage major mergers are not the primary formation mechanism for SMGs at $1 < z \lesssim 6$. Instead, other processes such as gas accretion and interactions likely play a significant role in driving the starburst phase in SMGs at different redshifts.

In conclusion, our study provides a comprehensive analysis of the size and merger fraction evolution of SMGs across a broad redshift range. The derived scaling relations and merger fraction trends offer valuable insights into the formation and evolution of these galaxies, highlighting the need for a multi-faceted approach to understanding their complex histories. Our findings underscore the importance of considering a range of physical processes, including but not limited to mergers, in shaping the properties of SMGs throughout cosmic history.

REFERENCES

Adscheid, S., Magnelli, B., Liu, D., et al. 2024, A&A, 685, A1

Alvarez-Marquez, J., Hashimoto, T., Arribas, S., et al. 2021, ALMA [OIII]88um Emitters. Signpost of Early Stellar Buildup and Reionization in the Universe, JWST Proposal. Cycle 1, ID. #1840, ,

An, F. X., Stach, S. M., Smail, I., et al. 2018, ApJ, 862, 101

An, F. X., Simpson, J. M., Smail, I., et al. 2019, ApJ, 886, 48

Barger, A. J., Cowie, L. L., Chen, C. C., et al. 2014, ApJ, 784, 9

Baugh, C. M., Lacey, C. G., Frenk, C. S., et al. 2005, MNRAS, 356, 1191

Belli, S., Conroy, C., Davies, R., et al. 2021, The Stellar and Gas Content of Galaxies at Cosmic Noon, JWST Proposal. Cycle 1, ID. #1810, ,

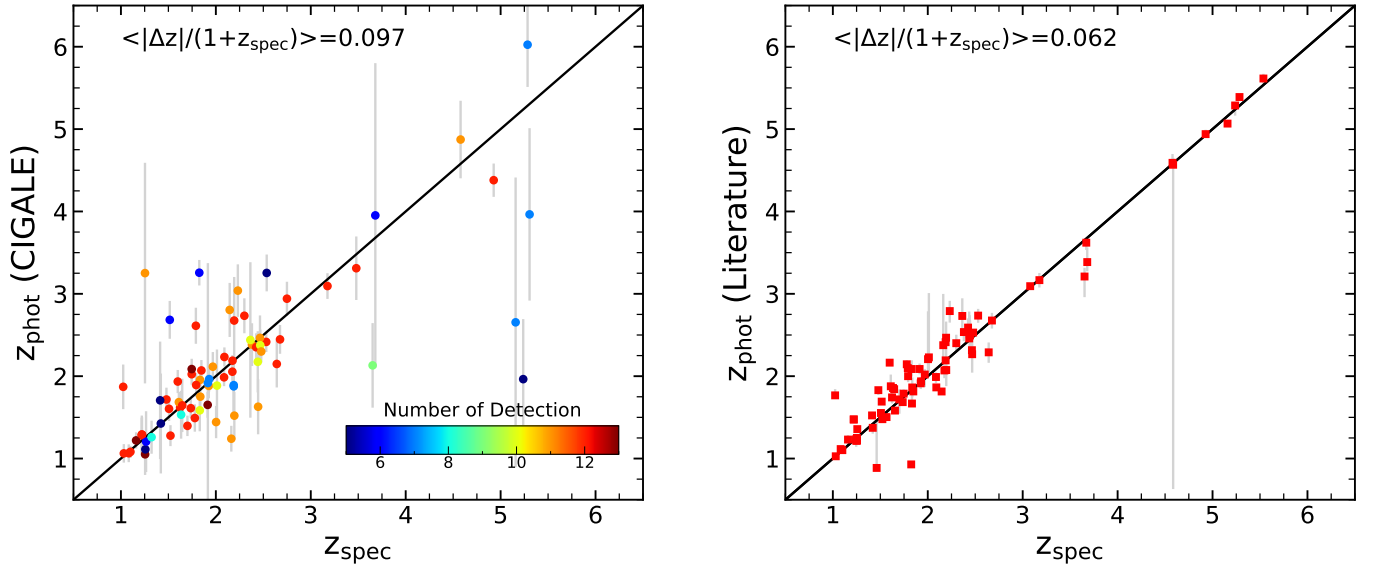Boogaard, L. A., Gillman, S., Melinder, J., et al. 2023, arXiv e-prints, arXiv:2308.16895

Boquien, M., Burgarella, D., Roehlly, Y., et al. 2019, A&A, 622, A103

Bradley, L., Sipőcz, B., Robitaille, T., et al. 2024, astropy/photutils: 1.12.0, v1.12.0, Zenodo, doi:10.5281/zenodo.10967176

Bruzual, G., & Charlot, S. 2003, MNRAS, 344, 1000

Calzetti, D., Armus, L., Bohlin, R. C., et al. 2000, ApJ, 533, 682

Chabrier, G. 2003, PASP, 115, 763

Chapman, S. C., Windhorst, R., Odewahn, S., Yan, H., & Conselice, C. 2003, ApJ, 599, 92

Charlot, S., & Fall, S. M. 2000, ApJ, 539, 718

Chen, C.-C., Smail, I., Swinbank, A. M., et al. 2015, ApJ, 799, 194

Cheng, C., Yan, H., Huang, J.-S., et al. 2022, ApJL, 936, L19

Cheng, C., Huang, J.-S., Smail, I., et al. 2023, ApJL, 942, L19

Conselice, C. J., Chapman, S. C., & Windhorst, R. A. 2003, ApJL, 596, L5

Conselice, C. J., Yang, C., & Bluck, A. F. L. 2009, MNRAS, 394, 1956

Cooper, O. R., Brammer, G., Heintz, K. E., et al. 2024, arXiv e-prints, arXiv:2410.08387

Crespo Gómez, A., Colina, L., Álvarez-Márquez, J., et al. 2024, arXiv e-prints, arXiv:2402.18672

Da Cunha, E., Charlot, S., & Elbaz, D. 2008, Monthly Notices of the Royal Astronomical Society, 388, 1595. https://doi.org/10.1111/j.1365-2966.2008.13535.x

Dale, D. A., Helou, G., Magdis, G. E., et al. 2014, ApJ, 784, 83

Dudzevičiūtė, U., Smail, I., Swinbank, A. M., et al. 2020, MNRAS, 494, 3828

Dunlop, J. S., Abraham, R. G., Ashby, M. L. N., et al. 2021, PRIMER: Public Release IMaging for Extragalactic Research, JWST Proposal. Cycle 1, ID. #1837, ,

Enia, A., Talia, M., Pozzi, F., et al. 2022, ApJ, 927, 204

Faber, S. 2011, The Cosmic Assembly Near-IR Deep Extragalactic Legacy Survey ("CANDELS"), STScI/MAST, , , doi:10.17909/T94S3X

Fritz, J., Franceschini, A., & Hatziminaoglou, E. 2006, MNRAS, 366, 767

Geda, R., Crawford, S. M., Hunt, L., et al. 2022, AJ, 163, 202

Gillman, S., Gullberg, B., Brammer, G., et al. 2023, A&A, 676, A26

Gillman, S., Smail, I., Gullberg, B., et al. 2024, arXiv e-prints, arXiv:2406.03544

Grogin, N. A., Kocevski, D. D., Faber, S. M., et al. 2011, ApJS, 197, 35

Hasinger, G., Capak, P., Salvato, M., et al. 2018, ApJ, 858, 77

Hayward, C. C., Narayanan, D., Kereš, D., et al. 2013, MNRAS, 428, 2529

Huang, J. S., Li, Z.-J., Cheng, C., et al. 2023, ApJ, 949, 83

Ilbert, O., Capak, P., Salvato, M., et al. 2009, ApJ, 690, 1236

Kartaltepe, J., Casey, C. M., Bagley, M., et al. 2021, COSMOS-Webb: The Webb Cosmic Origins Survey, JWST Proposal. Cycle 1, ID. #1727, ,

Kartaltepe, J. S., Dickinson, M., Alexander, D. M., et al. 2012, ApJ, 757, 23

Koekemoer, A. M., Faber, S. M., Ferguson, H. C., et al. 2011, ApJS, 197, 36

Kriek, M., Shapley, A. E., Reddy, N. A., et al. 2015, ApJS, 218, 15

Laigle, C., McCracken, H. J., Ilbert, O., et al. 2016, ApJS, 224, 24

Liu, D., Lang, P., Magnelli, B., et al. 2019, ApJS, 244, 40

Madau, P., & Dickinson, M. 2014, ARA&A, 52, 415

Martorano, M., van der Wel, A., Baes, M., et al. 2024, ApJ, 972, 134

McKinney, J., Casey, C. M., Long, A. S., et al. 2024, arXiv e-prints, arXiv:2408.08346

Michałowski, M. J., Dunlop, J. S., Koprowski, M. P., et al. 2017, MNRAS, 469, 492

Momcheva, I. G., Brammer, G. B., van Dokkum, P. G., et al. 2016, ApJS, 225, 27

Morishita, T., Mason, C., Trenti, M., et al. 2023, A NIRCam Pure-Parallel Imaging Survey of Galaxies Across the Universe, JWST Proposal. Cycle 2, ID. #3990, ,

Muzzin, A., Marchesini, D., Stefanon, M., et al. 2013, ApJS, 206, 8

Narayanan, D., Hayward, C. C., Cox, T. J., et al. 2010, MNRAS, 401, 1613

Narayanan, D., Turk, M., Feldmann, R., et al. 2015, Nature, 525, 496

Ormerod, K., Conselice, C. J., Adams, N. J., et al. 2024, MNRAS, 527, 6110

Pasha, I., & Miller, T. B. 2023, The Journal of Open Source Software, 8, 5703

Peng, C. Y., Ho, L. C., Impey, C. D., & Rix, H.-W. 2002, AJ, 124, 266

Qu, Y., Helly, J. C., Bower, R. G., et al. 2017, MNRAS, 464, 1659

Ren, J., Li, N., Liu, F. S., et al. 2023, ApJ, 958, 96

Riechers, D. A., Capak, P. L., Carilli, C. L., et al. 2010, ApJL, 720, L131

Rodriguez-Gomez, V., Snyder, G. F., Lotz, J. M., et al. 2019, MNRAS, 483, 4140

Schlawin, E., Leisenring, J., Misselt, K., et al. 2020, AJ, 160, 231

Simpson, J. M., Smail, I., Swinbank, A. M., et al. 2019, ApJ, 880, 43

Skelton, R. E., Whitaker, K. E., Momcheva, I. G., et al. 2014, ApJS, 214, 24

Smail, I., Chapman, S. C., Blain, A. W., & Ivison, R. J. 2004, ApJ, 616, 71

Smail, I., Ivison, R. J., Blain, A. W., & Kneib, J. P. 1998, ApJL, 507, L21

Smail, I., Morrison, G., Gray, M. E., et al. 1999, ApJ, 525, 609

Smail, I., Dudzevičiūtė, U., Gurwell, M., et al. 2023, ApJ, 958, 36

Smolčić, V., Karim, A., Miettinen, O., et al. 2015, A&A, 576, A127

Stach, S. M., Dudzevičiūtė, U., Smail, I., et al. 2019, MNRAS, 487, 4648

Swinbank, A. M., Smail, I., Chapman, S. C., et al. 2010, MNRAS, 405, 234

Tacconi, L. J., Neri, R., Chapman, S. C., et al. 2006, ApJ, 640, 228

Ueda, Y., Hatsukade, B., Kohno, K., et al. 2018, ApJ, 853, 24

Uematsu, R., Ueda, Y., Alexander, D. M., et al. 2024a, arXiv e-prints, arXiv:2412.09737

—. 2024b, arXiv e-prints, arXiv:2412.09737

Ward, E., de la Vega, A., Mobasher, B., et al. 2024, ApJ, 962, 176

Weaver, J. R., Kauffmann, O. B., Ilbert, O., et al. 2022, ApJS, 258, 11

Wiklind, T., Conselice, C. J., Dahlen, T., et al. 2014, ApJ, 785, 111

Wild, V., Charlot, S., Brinchmann, J., et al. 2011, MNRAS, 417, 1760

Yang, G., Boquien, M., Buat, V., et al. 2020, MNRAS, 491, 740

Yang, G., Boquien, M., Brandt, W. N., et al. 2022, ApJ, 927, 192

APPENDIX

A. THE PHOTOMETRY REDSHIFTS

Figure 7 shows the comparison of the $z_{\rm phot}$ obtained using CIGALE and the best $z_{\rm phot}$ obtained by Ren et al. (2023) using previous data with $z_{\rm spec}$.
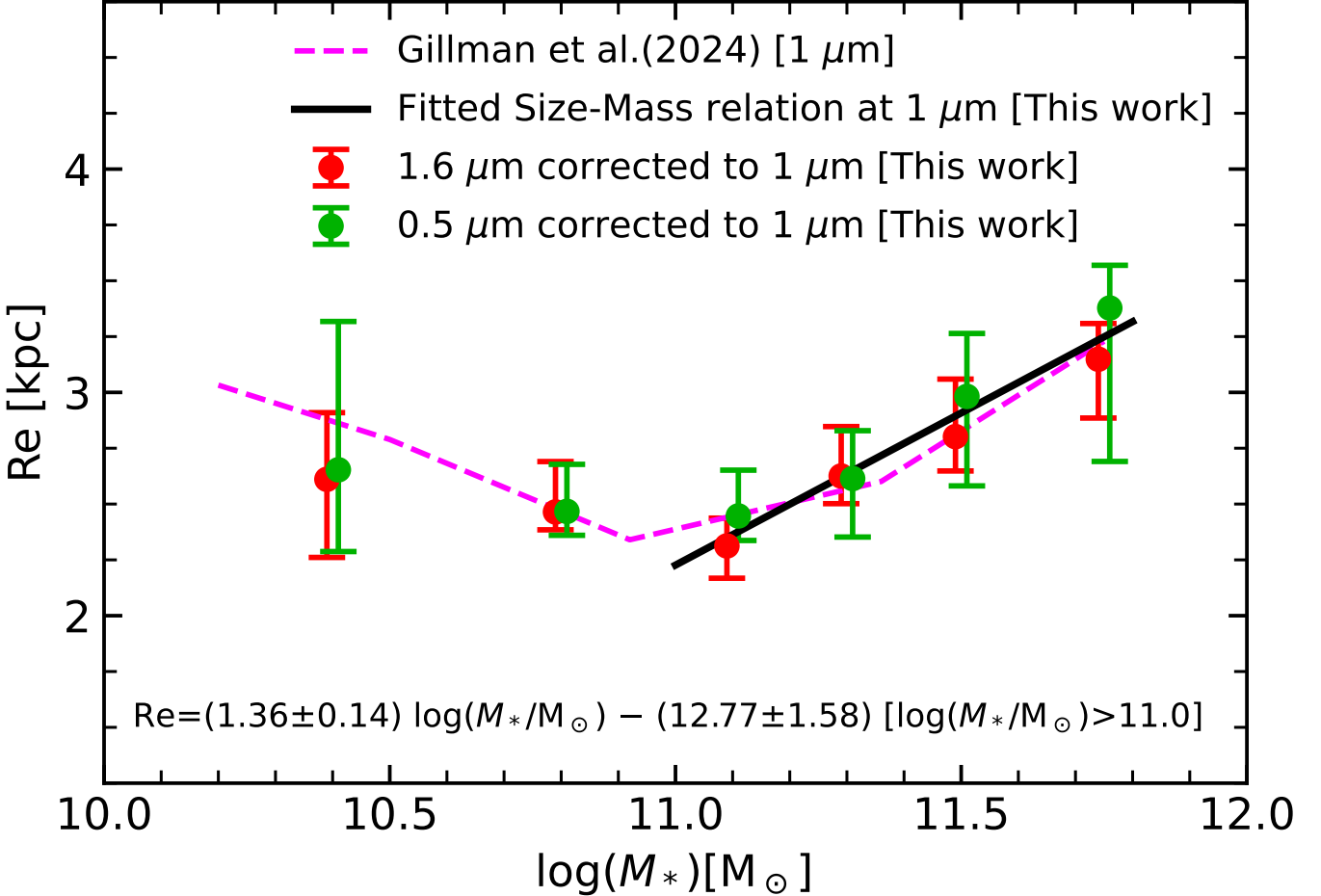

Figure 7. Left: comparison between spectroscopic redshift and photometric redshift estimated by CIGALE. Right: comparison between $z_{\rm spec}$ and $z_{\rm phot}$ in literature.
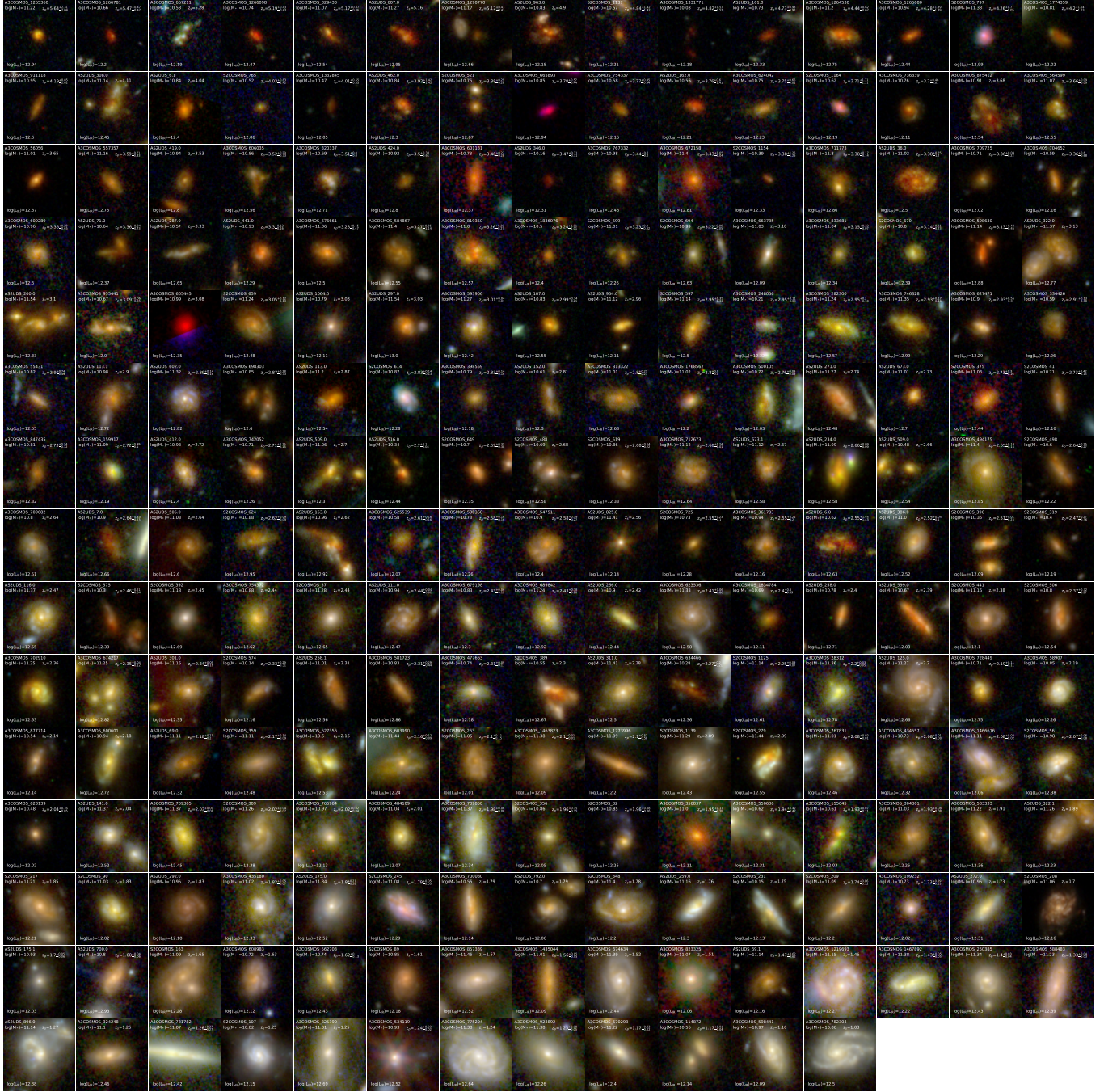
B. SIZE-MASS RELATION

We utilized the size evolution relationship with rest-frame wavelength provided by Gillman et al. (2024) to correct the $R_{\rm e}$ of our SMG sample to rest-frame $1\,\mu$m. Subsequently, accounting for an underestimation of approximately 0.2 dex in our stellar mass, we presented the size evolution with stellar mass in Figure 8. In the $\log(M_*/{\rm M}_\odot) > 10.5$ regime, our size-mass relation aligns with the one given by Gillman et al. (2024) . We fitted the size-mass relation for our sample at $\log(M_*/{\rm M}_\odot) > 11$, yielding $R_{\rm e} = (1.35 \pm 0.14)\,\log(M_*/{\rm M}_\odot)$ - (12.61±1.64).

C. THE IMAGES OF OUR SMG SAMPLE.

Figure 8. **The restframe 1 μm size versus the stellar mass of SMGs**. The magenta dashed line indicates the size-mass relation at 1 μm as given by Gillman et al. (2024) . The green and red points represent the median size of our sample corrected to 1 μ from rest-frame V and rest-frame NIR-band sizes in each stellar mass bin, respectively. The black solid line denotes the size-mass relation fitted using our data points.

J. Ren et al.

Figure 9. Pseudo-color images of the identified 222 SMGs. The ID, stellar mass, redshift, and infrared luminosity of each SMG are indicated at the top of its image. The images are arranged in redshift descending order. In each image, the physical size of the side length is 30 kpc.